Journal of Electron Spectroscopy and Related Phenomena 257 (2022) 147201

Contents lists available at ScienceDirect

Journal of Electron Spectroscopy and Related Phenomena

journal homepage: www.elsevier.com/locate/elspec

Observing structural distortions in complex oxides by x-ray photoelectron diffraction

Rosa Luca Bouwmeester, Thies Jansen [*], Marieke Altena, Gertjan Koster, Alexander Brinkman

Faculty of Science and Technology and MESA+ Institute for Nanotechnology, University of Twente, 7500 AE Enschede, The Netherlands

ARTICLE INFO

Keywords:
X-ray photoelectron diffraction
Complex oxides
Perovskites
Distortions
Oxygen displacement

ABSTRACT

The observation of structural distortions in complex oxides is becoming more important in order to explain their macroscopic behavior. X-ray photoelectron diffraction is an excellent technique to study the crystal structure and potentially observe oxygen distortions in an element-specific fashion. Its surface-sensitive character opens up the possibility to perform experiments on ultra-thin films without probing the substrate underneath. For $BaBiO_3$ thin films, for example recent experimental results point towards a suppression of an oxygen breathing mode with decreasing film thickness resulting in a decreased energy band gap. As another example, a nontrivial electronic band structure is predicted for [111]-bilayers of $LaMnO_3$. However, the likely presence of a Jahn–Teller distortion would suppress the topological phase. Here, the working principle of x-ray photoelectron diffraction is described and the data analysis required afterwards is discussed. X-ray photoelectron diffraction interference patterns are obtained for various thicknesses of $BaBiO_3$ and $LaMnO_3$ thin films. Experimental results are compared with multiple-scattering simulations. Although, indications for the structural distortions are observed, we discuss limitations of the technique in quantifying the displacement of the oxygen atoms.

1. Introduction

Structural distortions in complex oxides determine their macroscopic properties [1–3]. For example the magnetic anisotropy in $La_{1/3}Sr_{2/3}MnO_3$ [4] and $SrRuO_3$ [5,6], the influence on superconductivity in La_2CuO_4 [7] and ferromagnetism in $LaMnO_3$ [8]. Recently, a thickness-dependent band gap modification was observed in $BaBiO_3$ (BBO) thin films, caused by a suppression of the oxygen breathing mode [9]. Furthermore, a nontrivial band structure is predicted for a [111]-oriented bilayer of $LaMnO_3$ (LMO) [10] as long as the Jahn–Teller distortion is suppressed.

In order to gain more control and to enable the design of macroscopic material properties, accessible characterization of the structural distortions is essential. A technique often used for structural characterization is x-ray diffraction (XRD) [11–13]. As XRD is not surface sensitive [14], it is not so suitable to study the structural distortions in ultra-thin films. Previously, Raman spectroscopy and synchrotron diffraction experiments were combined to detect the thickness-dependent suppression of the breathing mode in BBO thin films [15], but a direct observation is still lacking. The Jahn–Teller distortion in LMO has been observed in synchrotron experiments [16], but is still challenging to be detected with an in-house lab setup.

In this work, we look into the possibility of observing the structural distortions using x-ray photoelectron diffraction (XPD), specifically focussing on the oxygen breathing mode in BBO and Jahn–Teller distortion in [111]-oriented LMO thin films. First, XPD is introduced as a technique. Second, the data analysis required is discussed by using a measurement on a Nb-doped $SrTiO_3$(001) (Nb:STO) substrate as an example. Subsequently, multiple-scattering simulations are introduced and compared to the experimental results. Finally, it is discussed how to confirm the presence and quantify the strength of the oxygen breathing mode and Jahn–Teller distortion in, respectively, BBO and LMO, by comparing experimental results and multiple-scattering simulations.

2. X-ray photoelectron diffraction

XPD is an element sensitive technique, which can be used to determine the crystal structure of a thin film. Originally, XPD is used to study the orientation of small molecules on a surface [17–19]. In more recent work, the structural transition from a planar- to chain-type $SrCuO_2$ crystal structure was observed upon decreasing film thickness by using XPD among other techniques [20] as well as the presence of the tetragonal structure in CuO thin films [21]. Also, the Cr or Ir doped $LaAlO_3/SrTiO_3$ interface has been studies by means of hard X-ray photoelectron diffraction [22]. Furthermore, for ultra-thin $PbTiO_3$ (PTO) films, the ferroelectric configuration was determined by combining

---

[*] Corresponding author.
E-mail address: t.jansen@utwente.nl (T. Jansen).

https://doi.org/10.1016/j.elspec.2022.147201
Received 4 November 2021; Received in revised form 4 April 2022; Accepted 5 April 2022

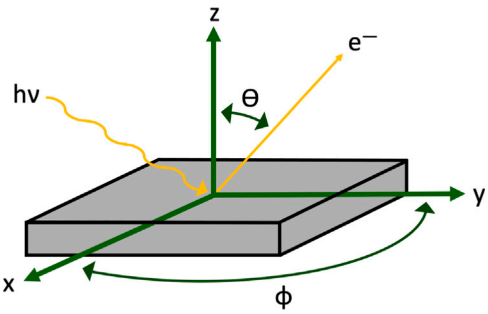

Fig. 1. The XPD system. A schematic drawing of the XPD setup, the degrees of freedom are indicated by the green arrows. The yellow arrows represent the incoming photon beam and outgoing photoelectrons.

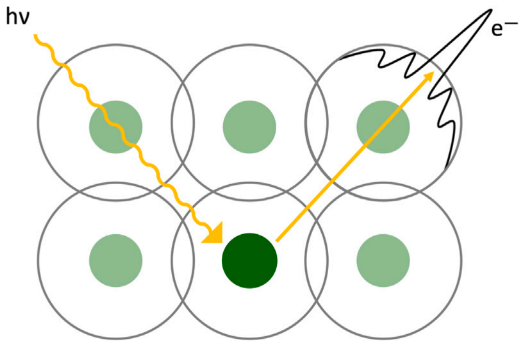

Fig. 2. Forward focussing is schematically depicted, adapted from [20]. The curvy yellow line shows the incoming photon beam and the dark green dot represent the emitting atom. The excited photoelectron (yellow arrow) interacts with the attractive potential of the neighboring atoms (the light green dots), resulting in an inference pattern (solid black line) with one outstanding peak: the forward focussing peak.

experimental and simulated XPD results [23,24]. In other fields, for example organic chemistry, XPD also proved to be useful when observing the light-induced *trans* to *cis* isomerization of azobenzene [25]. Despite its possibilities, the technique is not used often due to complexities in both the experimental setup and the data analysis.

In a very general picture, XPD can be described as angle-dependent x-ray photoelectron spectroscopy (XPS). In the '80s, XPD was even referred to as angle-resolved XPS in literature [17,26,27]. Just as in XPS, photoelectrons are generated by means of the photoelectric effect [18]. Both techniques are surface sensitive due to a limited mean escape depth (MED) of approximately 20 Å [23]. The MED depends on the material of interest and measurement conditions, such as the emission angle of the photoelectrons [28].

When inelastic scattering is ignored, the effective probing depth is calculated by [28,29]

$$I = I_0 e^{-d/\lambda \cos\theta} \tag{1}$$

with I the intensity originating from the emitted photoelectrons and Auger electrons [30], I_0 the original signal intensity (for example from a bare substrate), d the probing depth, λ the inelastic electron mean free path and θ the angle of the emitted photoelectron with respect to the surface normal [28,29].

From the measured kinetic energy (E_k) of the excited photoelectron, the element specific binding energy (E_b) of the emitting atom is calculated [31–34] by

$$E_k = h\nu - E_b - \Phi \tag{2}$$

where $h\nu$ is the energy of the incoming photons and Φ is the work function of the energy analyzer [29].

During an XPD measurement, the sample is rotated with respect to the analyser and around its own center, as schematically depicted in Fig. 1(a) by θ and ϕ, respectively, with the goal to probe the crystal structure. By rotating both the polar angle (θ) and the azimuthal angle (ϕ) during an XPD measurement, the whole upper hemisphere is probed. The angle between the x-ray source and electron analyzer is fixed. The technique remains element specific, since the photoelectric effect forms the basis and only photoelectrons with a specific kinetic energy are measured by the detector. By studying the intensity of photoelectrons as a function of sample orientation, the influence of the crystal structure on the excited photoelectron intensity is investigated — as explained in the subsequent subsection.

2.1. Forward focussing effect

In ordered systems, variations in the photoelectron intensity are observed due to coherent scattering [20,35]. In crystalline material systems, an increased intensity is observed along the nuclear axes because the emitted photoelectrons are attracted by the Coulomb potential of the neighboring atoms [26] and experience constructive interference [27]. This effect is called forward focussing and schematically depicted in Fig. 2.

After an incoming photon is absorbed by an atom (the emitter), a photoelectron wave is moving outwards in a certain direction. Since the neighboring atoms act as scatterers, constructive and destructive interference occurs between the direct and scattered waves [17,18,23,24,36,37]. When the kinetic energy of the emitted photoelectron exceeds a few hundred electronvolts, the scattering amplitude is mostly focussed in the forward direction leading to one outstanding peak in the interference pattern [18,23,26,27], see upper right corner in Fig. 2.

This peak can be directly associated with the position of the near-neighbors with respect to the emitter [19,24,27]: the closer the scatterers are located to the emitter, the larger the enhancement of the forward focussing peak [17]. The size of the neighboring atoms also has an influence, since a lower atomic number implies a lower scattering power [38]. The width of the forward focussing peak depends on the energy of the photoelectron: the higher the energy, the narrower the peak [20,26,35]. Furthermore, higher kinetic energies of the photoelectrons lead to improved focussing over larger nuclear distances [35]. So, when probing the crystal structure as a function of θ and ϕ, the highest photoelectron intensities will be found where most atoms are aligned, along the nuclear axes.

The interference pattern, see black line in Fig. 2, also provides structural information. The peak separation is, namely, determined by the interatomic distance and electron wavelength [18,35]. However, these peaks can also originate from interfering superpositions of contributions from smaller clusters and cannot easily be assigned to structural parameters, as is the case for the forward focussing peak. Furthermore, multiple-scattering events can cause a defocusing of the forward focussing peak and thus a decreased intensity [35] — making it challenging to identify if a peak is caused by interference or forward focussing. In that case, multiple-scattering simulations are a useful tool, as introduced in a subsequent section. Another effect that needs to be considered is the refraction of the scattered wave at the surface potential barrier [17], resulting in a more smeared out intensity of the forward focussing peak.

So, by rotating the sample in both θ and ϕ, the crystal structure is probed as a function of sample orientation with respect to the analyser. From the measured photoelectron intensity maxima, the surface crystal structure is resolved by determining the directions of the nuclear axes [35]. Since the detector is set to detect only photoelectrons with a specific kinetic energy, XPD is used to probe the local environment of a specific element. For a complete dataset, the XPD measurement is repeated for each element of interest, for which a specific core level is selected.

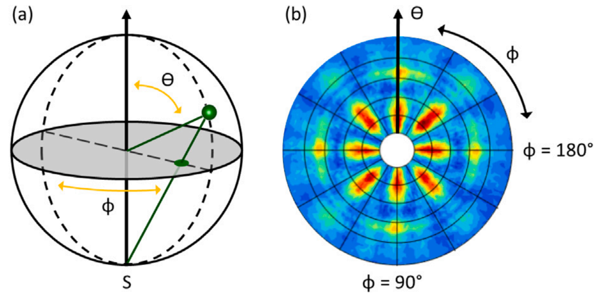

Fig. 3. (a) Schematically shown how a three-dimensional object, a sphere, is projected onto the equatorial plane (gray-shaded area). The green dot represents the point of interest, from where a line is drawn to the south pole. The point where the line intersects with the equatorial plane is the projection point. (b) An example of an XPD interference pattern. The polar and azimuthal dependencies are indicated by the arrows.

2.2. Details of the measurement setup

The XPD measurements were performed in an *in situ* Omicron Nanotechnology GmbH Surface Analysis system using a monochromatic Al Kα x-ray source with a kinetic energy of 1486.7 eV. By default the source was set to emission mode and a filament current of ~ 4.2 A. The typical background pressure was $2.0 \cdot 10^{-9}$ mbar. An EA 125 Energy Analyser, equipped with seven channeltron electron multipliers, was used to detect the excited photoelectrons. The angle between the x-ray source and the lens of the analyser is fixed by the geometry and equal to 80°.

The magnification of the analyser was set to a medium mode, corresponding to an angular acceptance of ± 4° and an analysis area with a diameter of 3.0 mm. The entrance aperture plate was set to 6 × 12 mm and the exit slits were 5 × 11 mm for each channeltron. Furthermore, a pass energy of 100 eV and a dwell time of 0.90 s were used. Typical step sizes in θ and ϕ are 3° for complete scans and 1° for high-resolution scans. For the latter, several polar angles are averaged for every azimuthal position.

The sample holder, used for XPD measurements, has the possibility of being cooled and heated in the temperature range of –134 °C to 227 °C. All results discussed in the remainder of this work are performed at room temperature.

3. Data analysis

After completion of an XPD measurement, analysis of the data is required before the final stereographic projection is obtained. In this section, the steps needed to obtain an accurate XPD interference pattern are described. As an example, a Nb:STO substrate (with a doping level of 0.5 wt%) is used to confirm the correctness of the measurement procedure and to demonstrate the influence of the steps taken during the data analysis. All the data analysis steps are performed in MATLAB.

3.1. Stereographic projections

A complete XPD dataset consists of an intensity measurement as a function of every unique combination of the polar angle (θ) and the azimuthal angle (ϕ) for every element of interest. In order to visualize this data, a stereographic projection is commonly used, which projects a three-dimensional object onto a two-dimensional plane [39].

During the XPD measurement the whole upper hemisphere is probed, so a sphere needs to be projected onto the two-dimensional plane — the equatorial plane. In Fig. 3(a) it is schematically shown how the sphere is projected onto the equatorial plane. The green dot represents the point of interest. From there, a line is drawn to the south pole of the sphere. The intersection point with the equatorial plane is where the point of interest is projected onto the two-dimensional image.

In Fig. 3(b), an example of an XPD interference pattern is shown, the polar and azimuthal dependencies are indicated. The center corresponds to normal emission (polar angle of $\theta = 0°$), the innermost ring to $\theta = 10°$ and the outermost ring to $\theta = 60°$. The high-intensity peaks relate to the nuclear axes of the crystal structure.

3.2. Data structure and normalization

At the start of an XPD measurement, one isolated core level for each element of interest is selected as well as one (or more) energy value(s) where no element peak is present. The latter will be used for an analysis step and from now on referred to as geometrical energy. To select the energy values, an XPS overview scan is taken, as presented in Fig. 4(a) for the Nb:STO substrate. The core levels O 1*s* (E_b = 530 eV), Ti 2*p* (E_b = 462 eV) and Sr 3*d* (E_b = 134.5 eV) and a geometrical energy of 934 eV are chosen. The step sizes for the polar and azimuthal angle are set to 2°.

For each core level, an energy region is determined in which no overlap with other core level peaks occurs and the complete peak is included, typical widths used vary between 10–40 eV. To cover the desired region, five measurements are performed at slightly different energy values close to the chosen core level energy. One makes then use of the spacial separation of the channeltron electron multipliers, which leads to the detection of photoelectrons with an offset in their kinetic energy compared to the energy detected by the channeltron in the center. Therefore, each measurement for each core level, at every unique combination of θ and ϕ, consists of 35 measurement points.

The rotations in θ and ϕ are controlled by motors, which follow a beforehand generated sequence file. At the start of the data analysis, one needs to account for the different sensitivities of the channeltron electron multipliers. To eliminate this effect, the sum of the photoelectrons measured with each individual channeltron at each position at the geometrical energy is used to normalize the channeltron count with respect to each other. After normalization, the data collected at $\theta = 56°$ and $\phi = 136°$ for the Ti 2*p* core level is plotted as an example in Fig. 4(b), shown by the black solid line.

In order to visualize the intensity solely originating from the forward focussed peak, two more analysis steps are required, as described below.

3.3. XPS background subtraction

Inelastic scattering effects give rise to a background in the photoelectron measurements [17]. To visualize the forward focussing peaks in a stereographic projection, it is desired to sum the intensity of only the peak at every measurement position and not any intensity originating from the background. Therefore, a background needs to be subtracted, for which the most straightforward manner is the subtraction of a linear fit [29,40].

For the data analysis of XPD, a linear background is subtracted at every position and for every element specific measurement [20]. For the example of the Ti 2*p* core level in Fig. 4(b), the gray dashed line denotes the linear fit and the green dashed line shows the intensity of the Ti 2*p* core level after subtracting the linear approximated background. The data points corresponding to the Ti 2*p* 3/2 plasmon-loss peak are excluded in the averaging procedure to determine the background. For the final stereographic projection, only the peak intensity is relevant. Therefore, the outermost data points are cut off and data analysis is continued for the solid dark green line in Fig. 4(b).

After subtracting the linear background, the intermediate results are visualized in stereographic projections, one for each core level, and presented in Fig. 5(a). Already, differences in the interference patterns for each element are noted. However, the data still needs to be corrected for the geometrical factor, as discussed subsequently.

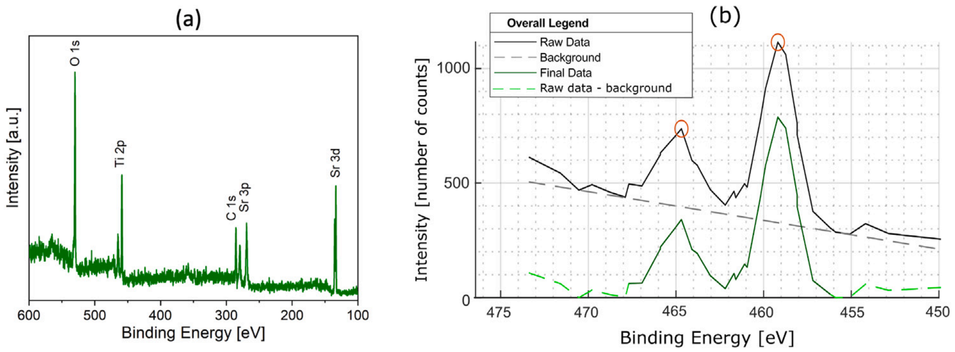

Fig. 4. (a) An XPS overview scan of a Nb:STO(001) substrate, showing the core level peaks used for the XPD measurement: O 1*s*, Ti 2*p*, Sr 3*d*. (b) An example of a measurement performed at every unique combination of θ and ϕ for every core level of interest — the Ti 2*p* peaks in this case for $\theta = 56°$ and $\phi = 136°$. The solid black line shows the data after channeltron normalization. The red dots indicated the peaks that were automatically found. The gray dashed line is the linear approximation of the inelastic scattering background. The green dashed line presents the data after subtraction of the linear background and the green solid line shows the final data used for further data analysis.

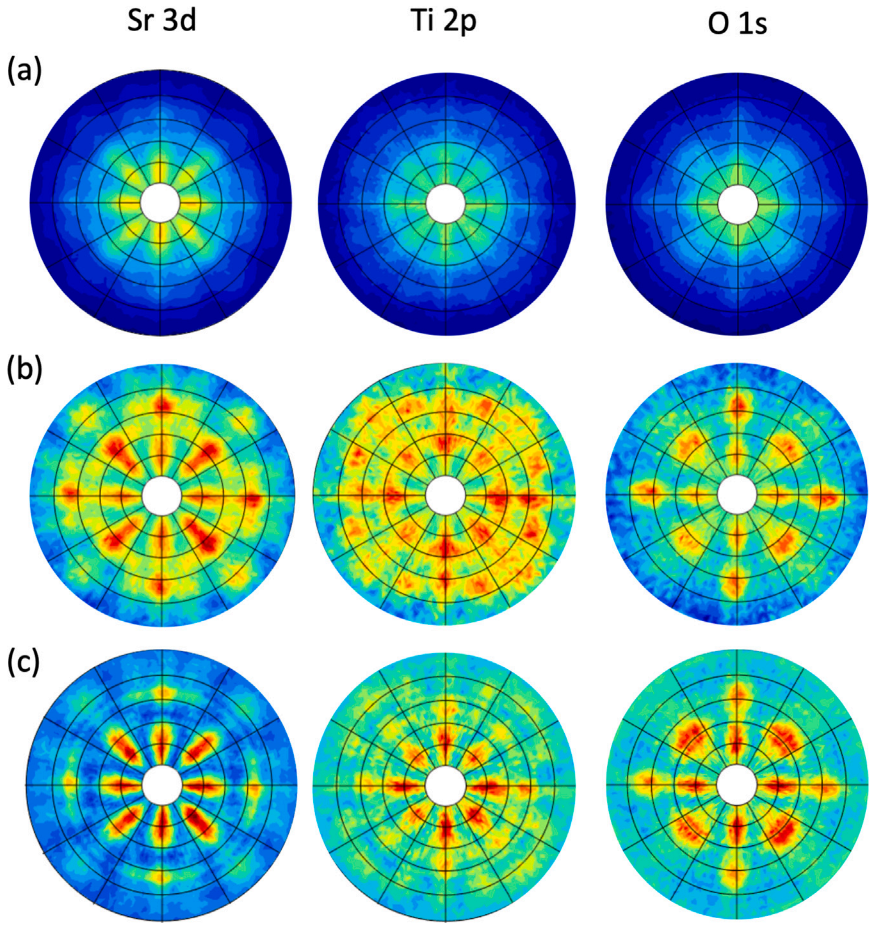

Fig. 5. Stereographic projection at various stages during the analysis of the XPD data obtained on Nb:STO. From left to right, the columns present the XPD interference patterns for the Sr 3d, Ti 2p and O 1s core levels. (a) After normalization of the channeltron electron multiplier count and subtraction of a linear background. (b, c) Final projections, when a correction for the geometrical factor has been made, in (b) the element specific data is divided by the geometrical energy measurement (method 1) and in (c) the scaled geometrical data is subtracted from the element specific data (method 2).

3.4. Correcting for the geometrical factor

The geometrical factor correction corrects for the angular influence of the setup, the possible misalignment of the sample with respect to the x-ray source and variations in the intensity of the x-ray source that might occur. The factors on which the intensity depends are given by [41]

$$I = nf\sigma\alpha(\theta)yA(\theta)T\lambda, \tag{3}$$

with n the number of atoms per cm^3, f the x-ray flux, σ is the cross-section, $\alpha(\theta)$ the angular correction factor, y the efficiency factor of the photoelectric effect, $A(\theta)$ the area from which the photoelectrons are detected, T the efficiency of the detector and λ, as in Eq. (1), the inelastic mean free path. When the sample is assumed to be homogeneous and the x-ray flux and efficiency of the process are constant, the two factors that remain of influence on the photoelectron intensity are the angular correction factor and the area of the sample that is probed.

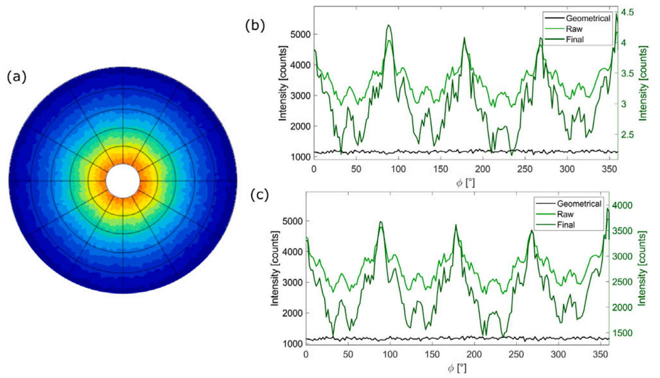

Fig. 6. (a) The measurement taken at the geometrical energy (E_b = 934 eV) for the STO substrate, visualized in a stereographic projection after channeltron normalization. (b, c) As an example, the data of the strontium atom at $\theta = 42°$ is taken. The light green line shows the element specific data after channeltron normalization and subtraction of a linear background, the dark green line the data corrected for the geometrical factor and the black line the geometrical measurement. The correction methods 1 and 2 are, respectively, applied for (b) and (c).

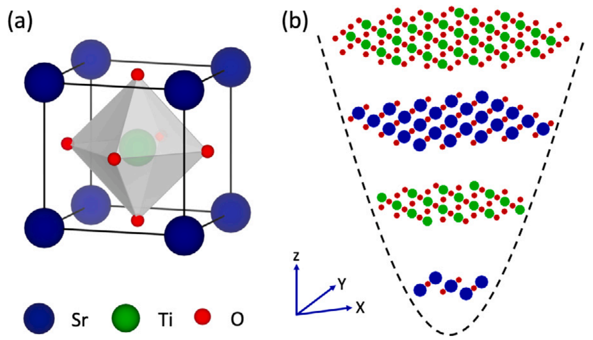

Fig. 7. (a) A schematic representation of the STO unit cell. (b) The TiO_2-terminated STO cluster used as input for multiple-scattering simulations, the parabolic cluster shape is indicated by the dashed black line. The vertical distances are much larger compared to the horizontal atomic distances. The atoms are not depicted in their realistic radii.

The measurement taken at the geometrical energy contains information on both of these factors and is presented in Fig. 6(a). When the sample is perfectly aligned, no intensity variations should occur for constant polar angles (from now on referred to as ϕ). The influence of the setup is always present, since the photoelectron count will be highest for normal emission ($\theta = 0°$) because the effective probing depth is the largest, as can also be deduced from Eq. (1). In Fig. 6(a), this angular dependence is clearly visible. The intensity for fixed polar angles is relatively constant, indicating a proper alignment of the sample.

The geometrical factor, referring to both sample misalignment as well as the angular dependence, is corrected for in various manners. More extensive reporting is found in [42]. Important requirements for the correction methods are that the positions of the peaks must not change upon correction and no peaks should (dis)appear. Here, two of the methods are discussed, both using the measurement taken at the geometrical energy:

1. Dividing the element specific data by the geometrical energy measurement.
2. Subtracting the scaled geometrical energy data from the element specific data.

For the first method, a corrected dataset is obtained by simply dividing each data point of the element specific measurement by the corresponding geometrical data points. This method is applied and shown in Fig. 6(b) for the strontium atoms at a position of $\theta = 42°$ as a function of ϕ. The light green line shows the data after channeltron normalization and subtraction of the linear background (raw data), the black line the geometrical data and the dark green line the data after the geometrical correction with method 1 (final data). Note that the corrected data corresponds to the right-hand y-axis. A clear fourfold symmetry is observed in both the raw and final data. Furthermore, the peak positions do not change upon correction and no peaks (dis)appear.

After correcting for the geometrical factor by method 1, the data is again visualized in a stereographic projection, presented in Fig. 5(b). The forward focussing peaks are much better visible than in Fig. 5(a) and the angular dependence in the intensity is reduced significantly. Additionally, the angular dependency can be reduced further by rescaling the corrected data for every polar angle position (a full ϕ-loop), as described in more detail in [42].

When the second method is applied, the geometrical data is subtracted from the element specific data. However, this cannot be done directly since the intensity difference is relatively large between the two as visualized in Fig. 6(c) by the light green and black lines, again for the strontium atom at $\theta = 42°$ as a function of ϕ. Therefore, the geometrical data is first scaled to the minimum intensity of the elemental data before the subtraction is performed. The scaling factor is determined for every position in θ, which could lead to a change in the relative intensities of the forward focussing peaks.

After scaling of the geometrical data to the element specific data, the first is subtracted from the latter, resulting in the dark green curve of Fig. 6(c) — note that the right-hand y-axis corresponds to the corrected data. The data is visualized in the stereographic projections presented in Fig. 5(c). For method 2, the angular dependence remains more pronounced than for method 1, unless a second scaling is applied for the final data.

In the final stereographic projections obtained with both methods, the fourfold symmetry of the STO substrate is clearly visible and earlier results are reproduced [20], indicating a successful data analysis. In the remainder of this work, it will be stated which correction method for the geometrical factor is used.

4. Multiple-scattering simulations

To help understand and interpret the XPD interference patterns, multiple-scattering simulations are performed using the electron diffraction in atomic clusters (EDAC) software [43]. The EDAC software approximates the atomic potentials by spherically symmetric muffin-tin potentials and is suitable for calculating the angular distribution of the photoelectrons in crystals as the multiple-scattering theory is implemented [43]. First, a finite cluster which describes the region that contributes to the emission of elastically scattered photoelectrons – limited by the electron inelastic mean free path – is included in the software. The use of clusters is suitable for simulating the XPD interference patterns, since short-range effects are dominant for the kinetic energies used [44]. Typical kinetic energies in this research are within the range of 400–1400 eV.

A STO unit cell and an example of a TiO_2-terminated STO cluster, consisting of 226 atoms, are shown in Fig. 7(a) and (b), respectively. The shape of the cluster was set to parabolic (indicated by the black dashed line) with a maximum distance of 13.6675 Å. Only the atoms whose distance to the emitter and to the surface is less than the maximum distance contribute to the intensity of emitted photoelectrons [43].

The stereographic projections shown in Fig. 8 visualize the result of the multiple-scattering simulations for the STO cluster, for which the same core levels were used as in the experimental XPD measurement. The number of emitters was 2, 1 and 5 for strontium, titanium and oxygen, respectively — all chosen symmetrically with respect to each other and at the center of the cluster. The simulated patterns are in

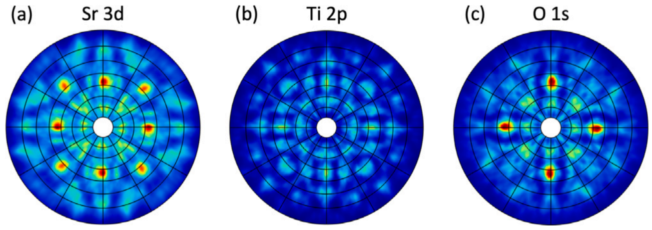

Fig. 8. The simulated XPD interference patterns of (a) Sr 3*d*, (b) Ti 2*p* and (c) O 1*s* using the EDAC software with the cluster depicted in Fig. 7(b) as input.

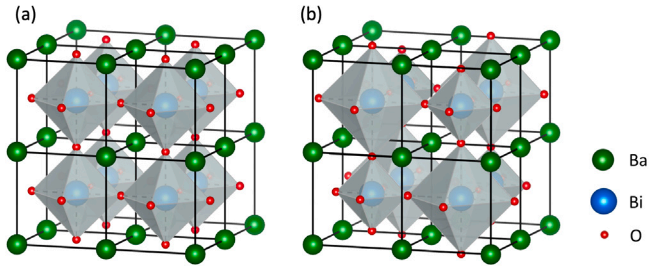

Fig. 9. The crystal structure of BBO schematically depicted. In (a) all oxygen octahedra have identical sizes. In (b) an oxygen breathing mode is present and the octahedra are alternately expanded and contracted around the Bi atom. The elements are indicated in the legend and not depicted in their realistic radii.

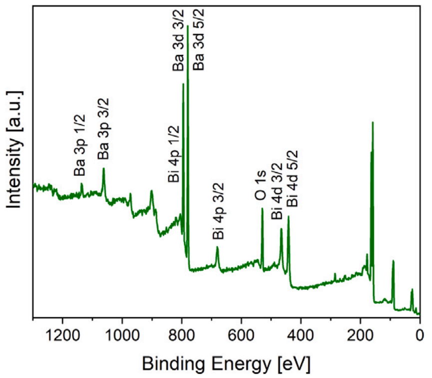

Fig. 10. XPS overview scan of the BBO film with a thickness of 30 u.c. The relevant core level peaks are indicated.

good agreement with the experimental results, presented in Fig. 5, and show a clear fourfold symmetry.

For the multiple-scattering simulations using EDAC, typical cluster sizes consist of ~200 atoms and a parabolic shape with a maximum distance of 13.6675 Å. The maximum total angular momentum was set to 15 and a maximum nuclear distance, which is defined as the maximum distance between two scattering events, was set to 1.8 nm. For a more elaborate explanation of the parameters, see the EDAC manual [45]. The inner potential and electron inelastic mean free path were set to 10.5 eV and 2.3 nm, respectively. These settings are similar as in previous work [20]. The number of iterations varied between 5 and 20, depending on when the results converged. All simulations are performed for T = 0 K and a Debye temperature of 100 K. Furthermore, a left circularly-polarized light source is chosen as an incident beam. However, since our experimental source is not circularly-polarized, the simulations are mirror symmetrized in ϕ afterwards.

5. Oxygen breathing mode in BaBiO$_3$

In this section, we discuss the oxygen octahedra breathing mode in BBO. A modification of the band gap size as a function of the BBO film thickness was observed by means of scanning tunneling spectroscopy (STS) experiments [9]. It is shown that the suppression of the oxygen breathing mode, defined by octahedra that expand and contract alternately around the Bi atom, is responsible for the decreasing band gap size upon decreasing film thickness. The BBO crystal structure without and with breathing mode is schematically depicted in Fig. 9(a) and (b), respectively.

The oxygen breathing mode is a structural and static distortion [46, 47] that causes a doubling of the unit cell parameters [15,48,49]. Therefore, it is expected that the oxygen breathing mode is directly observable using experimental techniques that characterize the crystal structure of a material system. The length scale at which the oxygen breathing mode takes places makes it, nevertheless, challenging. Recently published tight-binding (TB) models [50,51] show that a deviation of 0.1 Å with respect to the cubic position is already sufficient to open up an energy band gap in the electronic band structure. In the remainder of this work, the breathing mode strength (d [Å]) is defined as the deviation of the oxygen atoms with respect to the cubic position. Additionally, to observe the suppression of the oxygen breathing mode as a function of thickness, techniques that are sensitive for just a few monolayers are required. For both these reasons, XPD is a suitable technique to study the breathing mode as a function of thickness.

Here, two BBO thin films are studied with thicknesses that are expected to have a difference in the breathing mode strength from Ref. [9], namely 10 and 30 unit cells (u.c.). The BBO thin films studied are fabricated by PLD using Nb:STO substrates. The same growth conditions and parameters are used as in Ref. [52]. After fabrication, the BBO films are transferred *in situ* to the XPD measurement chamber.

The XPS overview scan is presented in Fig. 10 for the 30-unit-cell-thick BBO film. A small carbon core level peak is observed (E_b = 284.6 eV [53]), indicating a successful transfer. For the BBO film with a thickness of 10 u.c., the XPS spectrum is shown in the Supplementary Material. From these spectra the relevant core level peaks were chosen: Ba 3*d* 5/2 (E_b = 780 eV), Bi 4*d* 5/2 (E_b = 441 eV) and O 1*s* (E_b = 529 eV) and correct energy regions were determined. Geometrical energy measurements were performed at E_b = 850, 600 and 500 eV. Step sizes in the polar and azimuthal angle are set to 3° for complete scans. Subsequently, high-resolution scans are obtained for the aforementioned core levels and additionally for Ba 3*p* 3/2 (E_b = 1063 eV), with step sizes of 1° in θ and ϕ.

5.1. The oxygen breathing mode included in multiple-scattering simulations

Before the experimental XPD results are discussed, multiple-scattering simulations of the BBO structure with and without oxygen breathing mode are performed. All simulations were executed for BiO$_2$-terminated surfaces. Nevertheless, from experiments it is known that the BBO films no longer have single-terminated surfaces due to the presence of anti-phase boundaries in the films [52,54,55]. The simulations are performed for all four core levels stated before. By simulating both the Ba 3*p* 3/2 and 3*d* 5/2 core levels, the effect of kinetic energy on the XPD interference patterns is examined, as discussed in the Supplementary Material.

In the clusters used as input for the multiple-scattering simulations, the breathing mode was included by only taking into account the contraction and expansion of the octahedra — as it is previously shown that tilting of the octahedra was suppressed for BBO thin films [48]. From the schematic in Fig. 9, it is clear that the oxygen atoms move towards and away from the bismuth ion in the BiO$_2$ plane and down- and upwards in the BaO plane, for a contracted and expanded octahedron, respectively. Consequently, the symmetry of the environment of the Ba atom reduces from C_{4v} to C_{2v}.

The clusters used as input and the stereographic projections of the simulation results for the BBO structure in the absence and presence of the oxygen breathing mode are presented in Fig. 11 with d = 0.0 Å and d = 0.4 Å, respectively. In the distorted clusters, see Fig. 11(f) and

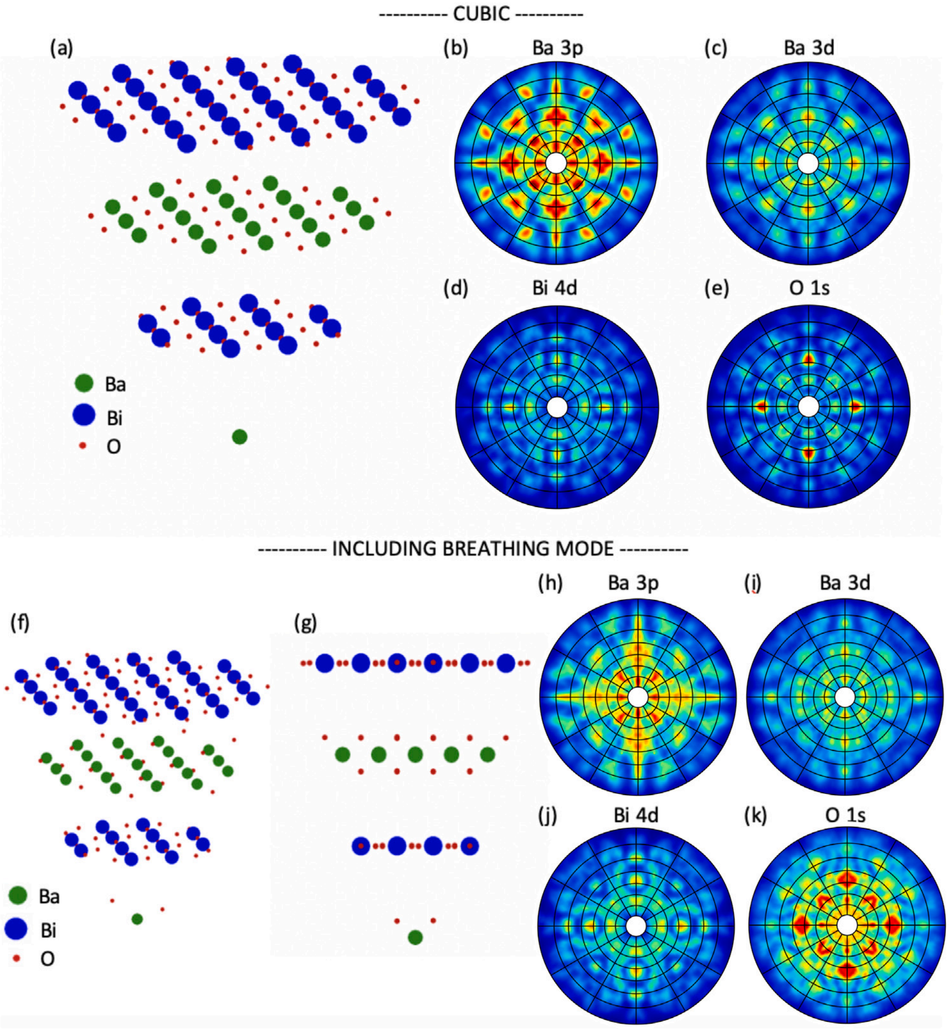

Fig. 11. The multiple-scattering simulation results for BBO in the absence (top) and presence (bottom) of the oxygen breathing mode. (a, f, g) Show the clusters used as input, with a BiO_2-terminated surface where in (g) the breathing mode is clearly visible by the horizontal displacement of the oxygen atoms in the BiO_2 plane and the vertical displacement in the BaO plane. The green, blue and red dots represent the barium, bismuth and oxygen atom, respectively. The atoms are not depicted in their realistic radii. Stereographic projections are shown for the (b, h) Ba 3*p*, (c, j) Ba 3*d*, (d, j) Bi 4*d* and (e, k) O 1*s* core levels. A breathing mode strength of d = 0.4 Å was included.

(g), the horizontal and vertical displacement of the oxygen atoms in the BiO_2 and BaO planes, respectively, is clearly visible. The clusters consists of 172 to 174 atoms, depending on which atom is chosen as center position within the cluster. The number of emitting atoms was set to 2, 1 and 4 for barium, bismuth and oxygen, respectively.

When comparing the stereographic projections with and without the breathing mode, presented in Fig. 11(b–e) and (h–k), respectively, minor differences are observed. By plotting the intensity as a ϕ-loop, the differences are better visualized. Fig. 12 presents the simulated and experimental intensity curves of the Ba 3*d* 5/2 core level at $\theta = 40°$. For the undistorted structure with $d = 0.0$ Å, a fourfold periodic intensity curve is observed, see the upper curve. When the oxygen breathing mode is included, with strengths of $d = 0.2$ Å and 0.4 Å, a twofold periodic intensity curve is observed, reflecting the reduction of the symmetry of the lattice from C_{4v} to C_{2v}. This effect becomes more apparent with increasing breathing mode strength. So, in the ideal case, distortions in the order of magnitude of 10 pm can be observed provided that they reduce the symmetry.

To gain more insight in the effect of the breathing mode on the XPD interference pattern, the BBO structure is schematically depicted in a two-dimensional fashion without and with the breathing mode present in Fig. 13(a) and (b), respectively. Forward focussing peaks are present along the nuclear axes and indicated by the blue arrows. In the absence of the breathing mode and with the barium atom as emitter, the oxygen atoms are aligned within the Ba–Ba forward focussing direction — resulting in the blue arrows in Fig. 13(a).

When the oxygen breathing mode is included, the fourfold symmetry in ϕ is reduced, as indicated by the blue arrows in Fig. 13(b). The oxygen atoms move away from the Ba–Ba nuclear axes upon inclusion of the breathing mode: the larger the breathing mode strength, the larger this deviation. Therefore, a reduction in the fourfold periodicity in ϕ as a function of breathing mode strength is expected, as observed in the multiple-scattering simulation results and indicated in Fig. 12.

A distortion which takes place at similar atomic displacement length scales as the oxygen breathing mode is the ferroelectric polar distortion in PTO [23,24]. When comparing the breathing mode in BBO with the up- and down-state in PTO, the main difference is that in PTO the distortions are within its unit cell and the same for every cell, while a doubling of the unit cell occurs for BBO. So, for PTO a shift of the forward focussing peak is observed in simulated interference patterns when comparing the up- and down-state, while for BBO additional forward focussing peaks appear upon inclusion of the oxygen breathing mode.

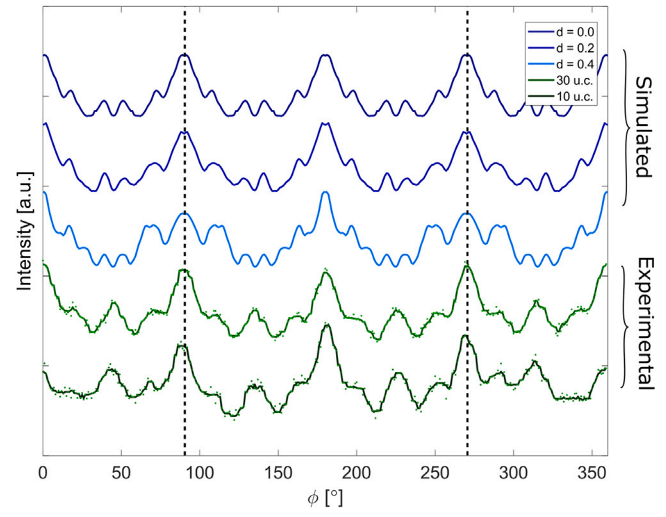

Fig. 12. Intensity curves of Ba 3d 5/2 core level as a function of ϕ for $\theta = 40°$. From dark to light blue, the multiple-scattering intensity curves are shown for d = 0.0 Å, 0.2 Å and 0.4 Å. The light and dark green curves show the experimental results from the high-resolutions scans (step sizes of 1° in θ and ϕ) for the 30 u.c. and 10 u.c. BBO films, respectively. The dots presents the data points averaged over θ = 38°–43°, the solid curve shows the smoothed data by taking the median value over a five-data-point sliding window. The red arrows indicate relative differences upon inclusion of the oxygen breathing mode and the black dashed lines indicated where signatures of the breathing mode appear.

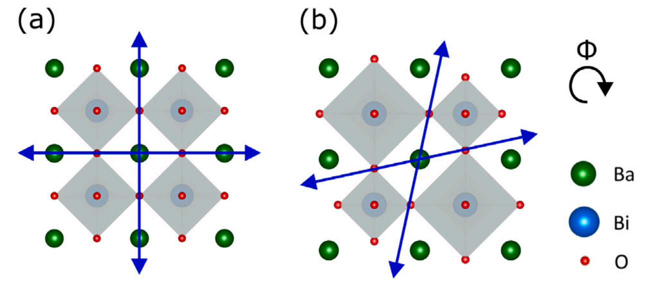

Fig. 13. The BBO structure (a) without and (b) with oxygen breathing mode (d = 0.15 Å) in a two-dimensional fashion. The blue arrows indicated the direction of the forward focussing peaks present in both cases when the barium atom is chosen as emitting atom. The yellow arrows indicate the additional forward focussing peaks caused by the breathing mode, these vary in azimuthal angle as a function of breathing mode strength. The elements are indicated in the legend and not depicted in their realistic radii, the gray-shaded areas represent the oxygen octahedra.

Furthermore, for PTO it is shown that Pb–Pb scattering dominates over Pb–O nuclear scattering [23], in good agreement with lower scattering powers for the oxygen atom compared to lead because of a lower atomic number [38]. The largest intensity peak in the ϕ-loops is, therefore, attributed to the forward focussing originating from the Ba–Ba scattering in BBO. The additionally appearing Ba–O forward focussing peaks upon increased breathing mode strength are less intense than the Ba–Ba forward focussing peak, in agreement with the results of PTO.

5.2. *BaBiO$_3$ films: 30 u.c. versus 10 u.c*

XPD measurements are performed on 30- and 10-unit-cell-thick BBO films and the complete scans are presented in Fig. 14(a) and (b), respectively. Method 2 was used to correct for the geometrical factor. The scaling of the geometrical energy data to the element specific data results in the difference in background intensity. All stereographic projections, except for the one of oxygen on the 10 u.c. BBO film, show clear fourfold symmetric interference patterns. Similarities with, especially, the undistorted BBO simulated interference patterns are present.

As for the multiple-scattering simulation results, comparing results with solely the stereographic projections is challenging. Similarly, ϕ-loops cross-sections are presented in Fig. 12 by the light and dark green curves for the 30 u.c. and 10 u.c. BBO films, respectively. For the experimental results, high-resolution scans for the Ba 3d 5/2 core level are taken for θ = 38°–43° and for ϕ = 0°–360°, with step sizes of 1° in both angular degrees of freedom. A geometrical energy measurement taken at E_b = 1000 eV was used to correct for the geometrical factor using method 2. The presented ϕ-loops are obtained by averaging over the six polar angles, as presented by the green dots in Fig. 12. Subsequently, the data is smoothed by a five-data-point sliding window, shown by the solid green curves.

For the high-resolution scans on the 10-unit-cell-thick BBO film, a large intensity variation was present in the geometrical energy measurement. Even by correcting for the geometrical factor, the effect remained present in the final result, as is visible for $\phi > 310$ and $\phi < 50$ of the dark green curve in Fig. 12. Between ϕ = 90°–270°, the variation in geometrical intensity is minimal. The intensity variations in the ϕ-loops for the 10 u.c. and 30 u.c. BBO films are almost identical. The reduction in the symmetry that occurred in the multiple-scattering simulations when the oxygen breathing mode was included, is absent in both experimental results. This indicates that the oxygen breathing mode is absent, or that the breathing mode is not homogeneous throughout the film, i.e. different domains are probed during the experiment.

6. Jahn-Teller distortions in LaMnO$_3$

Another distortion of interest is the Jahn–Teller distortion, which together with an $a^+b^-b^-$ rotation pattern, lowers the symmetry from cubic to orthorhombic in bulk LMO [16]. When a LMO thin film is fabricated along the [111]-direction with a thickness of 2 u.c., a buckled honeycomb structure is formed. This geometry in combination with spin–orbit coupling is theoretically predicted to possess nontrivial topological phases [10,56]. The Jahn–Teller distortion is predicted to suppress this topological phase in a [111]-oriented LMO bilayer [10, 57]. However, experimentally it might be possible to suppress the Jahn–Teller distortion by means of strain or substrate effects and engineer a topological insulating phase [4,58]. Therefore, it is desired to be able to study the structural phase of LMO thin films down to two unit cells. Here we present our findings of an XPD study on a 20 nm thick LMO thin film grown with pulsed laser deposition on a [111]-oriented LaAlO$_3$ substrate.

To study the structural phase of a LMO thin film, multiple-scattering simulations are done in order to interpret the experimental results. In the simulations the temperature is set to 293 K and the Debye temperature is set to 100 K. Two types of clusters are used: a cubic cluster and a orthorhombic cluster, in which the z-axis corresponds to the (111) (pseudo cubic) crystal axis. The lattice parameter of the cubic cluster is set to 3.944 Å. For the orthorhombic cluster the structural parameters from Ref. [16] are used. For the cubic cluster, a three-fold symmetric ϕ dependency is expected. For the orthorhombic cluster on the other hand, there is no symmetry expected in the ϕ dependency, since the a, b and c pseudo cubic lattice parameters are all different. However, experimentally one would not expect the complete film to be a single domain, but multiple domains rotated 120° with respect to each other. To incorporate this in the simulations the results of the orthorhombic cluster are symmetrized according to the C_{3v} point group.

Fig. 15 shows the simulations for the cubic and orthorhombic cluster for $\theta = 36°$. Fig. 15 also shows the experimental ϕ dependence averaged over a θ band of 34–38°. All the three elements present in the film, La, Mn and O are shown.

First of all, the difference between the cubic and orthorhombic multiple-scattering simulations is small. For La, the peaks at ϕ =

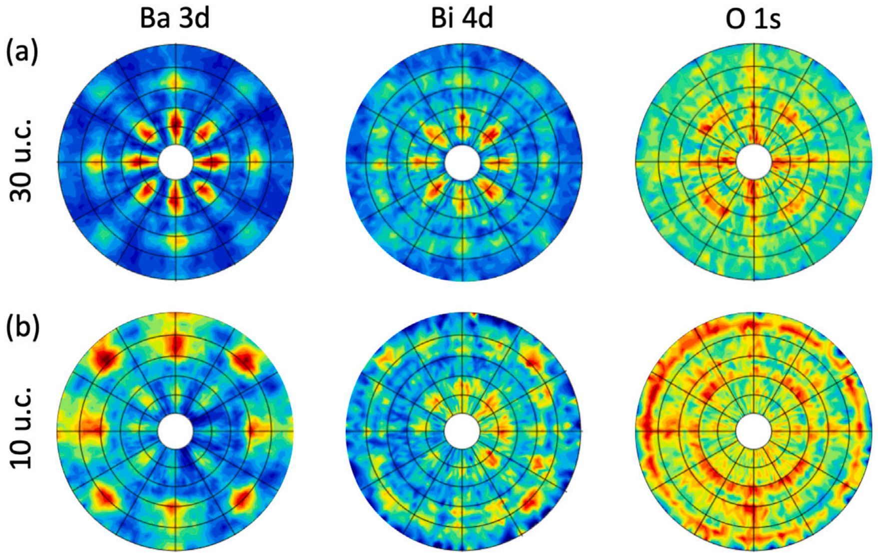

Fig. 14. Experimental XPD results of BBO thin films with a thickness of (a) 30 u.c. and (b) 10 u.c. From left to right, the Ba 3*d* 5/2 (E_b = 780 eV), Bi 4*d* 5/2 (E_b = 441 eV) and O 1*s* (E_b = 529 eV) XPD interference patterns are presented. The step sizes in θ and ϕ are 3°.

$0°, 120°, 240°$ seems suppressed in the orthorhombic phase. However, for Mn and O the ϕ dependence is almost identical to the cubic phase. Second, the experimental data shows good agreement with the simulated data, confirming the presence of the perovskite phase. However, the resolution of the experimental setup limits further refinement of the crystal structure. The resolution is limited by the intensity of the source, the inaccuracy of the motors and the large spot size of the source.

Two scenarios are possible. The first scenario is that the LMO film is orthorhombic (or some other lower symmetry phase than cubic), but consists of multiple domains oriented 120° with respect to each other. In this case the multiple domains will average out the nonsymmetric orthorhombic signal to be three-fold symmetric. The second scenario would be that the LMO film is indeed cubic and consist of a single domain.

So, Jahn–Teller distortions could not be distinguished. Nevertheless, this example shows how structural information can be extracted with XPD and a good agreement of the simulations with the experimental data.

7. Conclusions

The presented results of the STO substrate, BBO and LMO thin films show that XPD is a useful technique to determine the crystal structure of the material system. Even for ultra-thin films, interference patterns with significant intensity differences are observed. More details of the interference patterns are visualized by plotting the results as ϕ-loops.

XPD interference patterns were simulated for breathing mode strengths of d = 0.2 Å and 0.4 Å, which is relatively large compared to the theoretical value of d = 0.1 Å [50,51]. However, the differences between the simulated results were minor. The reduction of the symmetry from fourfold to twofold in the multiple-scattering simulations upon inclusion of the oxygen breathing mode reflects the reduction of the symmetry of the crystal when the breathing mode is present.

The experimental stereographic projections and ϕ-loops of the 10- and 30-unit-cell-thick BBO films showed many similarities with the results of the multiple-scattering simulations. The main argument for the presence of the oxygen breathing mode is a reduction of the fourfold symmetry to twofold. However, this twofold symmetry is not observed, so this would indicate the absence of the breathing mode or the presence of the breathing mode in different domains oriented 90 degrees with respect to each other. In the latter case it is still hard to quantify the strength of the breathing mode, since the relative contribution of each domain type is unknown.

Further, the ϕ-loops for 20 nm thick LMO films reveal good agreement with the multiple-scattering simulations. However, from the simulations no clear difference between the cubic and orthorhombic phase is revealed. Therefore, it is hard to determine the structural phase of the LMO film based on these measurements. The measurements could not be used to further differentiate between a multi-domain orthorhombic structure or a single-cubic domain.

Multiple-scattering simulations are very useful tool and should ideally be performed before experiments are executed. Using the simulated interference patterns, one could estimate whether the effect of interest is observable in experiments. Some distortions, like the transition from up- to down-state in PTO [23,24], are more suitable to observe with XPD than others.

To be able to observe distortions on the atomic scale, improvements in the XPD setup could be made. For example by decreasing the spot size, which is currently 3.0 mm in diameter. The XPD setup can also to be cooled down and heated, opening up the possibility to study structural transitions as a function of temperature, for example the rutile to monoclinic phase transition in VO_2 [59].

In conclusion, XPD is a useful technique for determining the crystal structure of ultra-thin films, but it is challenging to structurally observe distortions that take place at length scales below ~10 pm.

Acknowledgments

We would like to acknowledge Dominic Post for his technical support. This work is supported by NWO through a VICI grant and the project TOPCORE.

Appendix A. Supplementary data

Supplementary material related to this article can be found online at https://doi.org/10.1016/j.elspec.2022.147201.

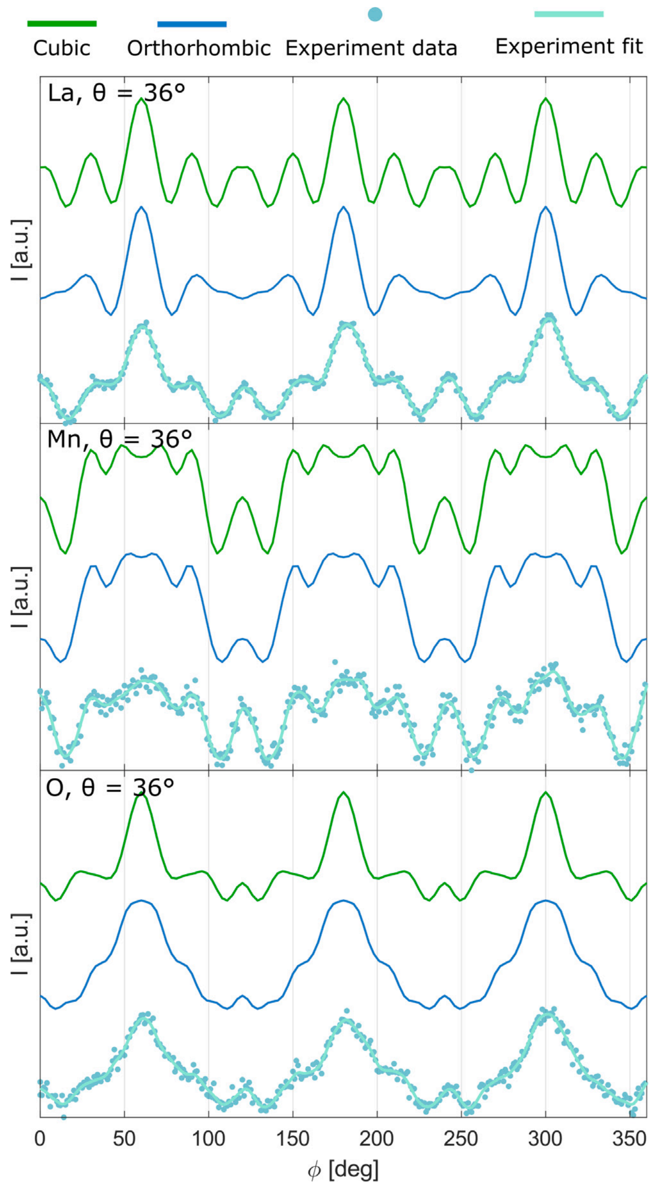

Fig. 15. ϕ dependency for simulated cubic and orthorhombic cluster, experimental data and fit to experimental data for elements La, Mn, and O.

References

[1] H.Y. Hwang, Y. Iwasa, M. Kawasaki, B. Keimer, N. Nagaosa, Y. Tokura, Emergent phenomena at oxide interfaces, Nature Mater. 11 (2) (2012) 103–113.

[2] Y. Suyolcu, G. Christiani, P. van Aken, G. Logvenov, Design of complex oxide interfaces by oxide molecular beam epitaxy, J. Supercond. Nov. Magn. 33 (1) (2020) 107–120.

[3] H. Banerjee, Understanding the role of exchange and correlations in complex oxides under strain and oxide heterostructures, Modern Phys. Lett. B 34 (23) (2020) 2030006.

[4] Z. Liao, M. Huijben, Z. Zhong, N. Gauquelin, S. Macke, R. Green, S. Van Aert, J. Verbeeck, G. Van Tendeloo, K. Held, et al., Controlled lateral anisotropy in correlated manganite heterostructures by interface-engineered oxygen octahedral coupling, Nature Mater. 15 (4) (2016) 425–431.

[5] R. Aso, D. Kan, Y. Shimakawa, H. Kurata, Control of structural distortions in transition-metal oxide films through oxygen displacement at the heterointerface, Adv. Funct. Mater. 24 (33) (2014) 5177–5184.

[6] D. Kan, R. Aso, R. Sato, M. Haruta, H. Kurata, Y. Shimakawa, Tuning magnetic anisotropy by interfacially engineering the oxygen coordination environment in a transition metal oxide, Nature Mater. 15 (4) (2016) 432–437.

[7] Y.E. Suyolcu, Y. Wang, W. Sigle, F. Baiutti, G. Cristiani, G. Logvenov, J. Maier, P.A. van Aken, Octahedral distortions at high-temperature superconducting La_2CuO_4 interfaces: visualizing Jahn–Teller effects, Adv. Mater. Interfaces 4 (24) (2017) 1700737.

[8] X.R. Wang, C.J. Li, W.M. Lü, T.R. Paudel, D.P. Leusink, M. Hoek, N. Poccia, A. Vailionis, T. Venkatesan, J.M.D. Coey, E.Y. Tsymbal, Ariando, H. Hilgenkamp, Imaging and control of ferromagnetism in $LaMnO_3/SrTiO_3$ heterostructures, Science 349 (6249) (2015) 716–719.

[9] R.L. Bouwmeester, A. Brinkman, K. Sotthewes, Thickness-dependent band gap modification in $BaBiO_3$, Nano- Mater. 11 (2021) 4.

[10] D. Doennig, S. Baidya, W.E. Pickett, R. Pentcheva, Design of Chern and Mott insulators in buckled 3*d* oxide honeycomb lattices, Phys. Rev. B 93 (2016) 165145.

[11] J. Hook, H. Hall, Solid State Physics, Manchester Physics Series, Wiley, 2013.

[12] J. Als-Nielsen, D. McMorrow, Elements of modern X-ray physics, John Wiley & Sons, 2011.

[13] C. Suryanarayana, M.G. Norton, X-ray diffraction: a practical approach, Springer Science & Business Media, 2013.

[14] C. Giannini, M. Ladisa, D. Altamura, D. Siliqi, T. Sibillano, L. De Caro, X-ray Diffraction: a powerful technique for the multiple-length-scale structural analysis of nanomaterials, Crystals 6 (8) (2016) 87.

[15] G. Kim, M. Neumann, M. Kim, M.D. Le, T.D. Kang, T.W. Noh, Suppression of three-dimensional charge density wave ordering via thickness control, Phys. Rev. Lett. 115 (2015) 226402.

[16] J. Rodríguez-Carvajal, M. Hennion, F. Moussa, A.H. Moudden, L. Pinsard, A. Revcolevschi, Neutron-diffraction study of the Jahn-Teller transition in stoichiometric $LaMnO_3$, Phys. Rev. B 57 (1998) R3189–R3192.

[17] S. Kono, S. Goldberg, N. Hall, C. Fadley, Chemisorption geometry of c(2× 2) oxygen on Cu(001) from angle-resolved core-level x-ray photoemission, Phys. Rev. B 22 (12) (1980) 6085.

[18] R. Fasel, P. Aebi, X-ray Photoelectron diffraction: probing atom positions and molecular orientation at surfaces, CHIMIA Int. J. Chem. 56 (10) (2002) 566–572.

[19] C.S. Fadley, X-ray Photoelectron diffraction, in: Physics of Solid Surfaces 1987, in: Studies in Surface Science and Catalysis, Elsevier, 1988.

[20] B. Kuiper, Size Effects in Epitaxial Oxide Thin Films (Ph.D. thesis), University of Twente, the Netherlands, 2014.

[21] W. Siemons, G. Koster, D.H. Blank, R.H. Hammond, T.H. Geballe, M.R. Beasley, Tetragonal cuo: End member of the 3*d* transition metal monoxides, Phys. Rev. B 79 (19) (2009) 195122.

[22] M. Lee, X.L. Tan, M. Yoneda, T. Okamoto, I. Tanaka, Y. Higa, D. Peng, M. Ogi, S. Kobayashi, M. Taguchi, M. Lippmaa, M.-J. Casanove, H. Daimon, Distortion analysis of Ir- and Co-doped LaAlO3/SrTiO3 (001) interfaces by hard X-ray photoelectron diffraction, J. Phys. Soc. Japan 87 (8) (2018) 084601.

[23] L. Despont, C. Koitzsch, F. Clerc, M. Garnier, P. Aebi, C. Lichtensteiger, J.-M. Triscone, F.G. de Abajo, E. Bousquet, P. Ghosez, Direct evidence for ferroelectric polar distor- tion in ultrathin lead titanate perovskite films, Phys. Rev. B 73 (9) (2006) 094110.

[24] L. Despont, C. Lichtensteiger, F. Clerc, M. Garnier, F.G. de Abajo, M. Van Hove, J.-M. Triscone, P. Aebi, X-ray Photoelectron diffraction study of ultrathin $PbTiO_3$ films, Eur. Phys. J. B 49 (2) (2006) 141–146.

[25] A. Schuler, M. Greif, A. Seitsonen, G. Mette, L. Castiglioni, J. Osterwalder, M. Hengsberger, Sensitivity of photoelectron diffraction to conformational changes of adsorbed molecules: Tetra-tert-butyl-azobenzene/ Au(111), Struct. Dynam. 4 (1) (2017) 015101.

[26] H. Poon, S. Tong, Focusing and diffraction effects in angle-resolved x-ray photoelectron spectroscopy, Phys. Rev. B 30 (10) (1984) 6211.

[27] W. Egelhoff Jr., X-ray Photoelectron and auger-electron forward scattering: A new tool for studying epitaxial growth and core-level binding-energy shifts, Phys. Rev. B 30 (2) (1984) 1052.

[28] C. Powell, A. Jablonski, Surface sensitivity of X-ray photoelec- tron spectroscopy, Nucl. Instrum. Methods Phys. Res. A 601 (1–2) (2009) 54–65.

[29] G. Greczynski, L. Hultman, X-ray Photoelectron spectroscopy: Towards reliable binding energy referencing, Prog. Mater. Sci. 107 (2020) 100591.

[30] C.C. Chang, Auger electron spectroscopy, Surf. Sci. 25 (1) (1971) 53–79.

[31] J.M. Hollander, W.L. Jolly, X-ray Photoelectron spectroscopy, Acc. Chem. Res. 3 (6) (1970) 193–200.

[32] C.C. Chusuei, D.W. Goodman, X-ray photoelectron spectroscopy, in: Encyclopedia of Physical Science and Technology, Vol. 17, Academic Press NY, 2002, pp. 921–938.

[33] A. Damascelli, Probing the electronic structure of complex systems by ARPES, Phys. Scr. 2004 (T109) (2004) 61.

[34] T. Rödel, Two-Dimensional Electron Systems in Functional Oxides Studied by Photoemission Spectroscopy (Ph.D. thesis), Université Paris- Saclay, *Université Paris- Saclay*, France, 2016.

[35] M.-L. Xu, M. Van Hove, Surface structure determination with forward focused electrons, Surf. Sci. 207 (2–3) (1989) 215–232.

[36] T. Matsushita, F. Matsui, K. Goto, T. Matsumoto, H. Daimon, Element assignment for three-dimensional atomic imaging by photoelectron holography, J. Phys. Soc. Japan 82 (11) (2013) 114005.

[37] X. Liang, C. Lubin, C. Mathieu, N. Barrett, Processing and analysis of X-ray photoelectron diffraction data using IGOR Pro, J. Appl. Crystallogr. 51 (3) (2018) 935–942.

[38] B. Warren, B. Averbach, B. Roberts, Atomic size effect in the x-ray scattering by alloys, J. Appl. Phys. 22 (12) (1951) 1493–1496.

[39] M. De Graef, M.E. McHenry, Structure of Materials: an Introduction to Crystallography, Diffraction and Symmetry, Cambridge University Press, 2012.

[40] J. Végh, The shirley background revised, J. Electron Spectrosc. Relat. Phenom. 151 (3) (2006) 159–164.

[41] C. Wagner, Sensitivity factors for XPS analysis of surface atoms, J. Electron Spectrosc. Relat. Phenom. 32 (2) (1983) 99–102.

[42] M. Altena, Bachelor Thesis – X-Ray Photoelectron Diffraction: Improving Measurements and Optimizing the Data Analysis in MATLAB, University of Twente, the Netherlands, 2020.

[43] F.G. de Abajo, M. Van Hove, C. Fadley, Multiple scattering of electrons in solids and molecules: A cluster-model approach, Phys. Rev. B 63 (7) (2001) 075404.

[44] A. Winkelmann, C.S. Fadley, F.J.G. de Abajo, High-energy photoelectron diffraction: model calculations and future possibilities, New J. Phys. 10 (11) (2008) 113002.

[45] Manual for multiple-scattering simulations using electron diffraction in atomic clusters (EDAC), 2021, http://garciadeabajos-group.icfo.es/widgets/edac/manual/edac.html. (Accessed: 05 April 2021).

[46] R.P. Lobo, F. Gervais, Bismuth disproportionation in $BaBiO_3$ studied by infrared and visible reflectance spectra, Phys. Rev. B 52 (1995) 13294–13299.

[47] H.G. Lee, R. Kim, J. Kim, M. Kim, T.H. Kim, S. Lee, T.W. Noh, Anisotropic suppression of octahedral breathing distortion with the fully strained $BaBiO_3/BaCeO_3$ heterointerface, APL Mater. 6 (1) (2018) 016107.

[48] K. Inumaru, H. Miyata, S. Yamanaka, Partial suppression of structural distortion in epitaxially grown $BaBiO_3$ thin films, Phys. Rev. B 78 (2008) 132507.

[49] J. Ge, W.-J. Yin, Y. Yan, Solution-processed Nb-substituted $BaBiO_3$ double perovskite thin films for photoelectrochemical water reduction, in: Chem. Mater., Chem. Mater. 30 (3) (2018) 1017–1031.

[50] A. Khazraie, K. Foyevtsova, I. Elfimov, G.A. Sawatzky, Oxygen holes and hybridization in the bismuthates, Phys. Rev. B 97 (2018) 075103.

[51] A.E. Lukyanov, I.A. Kovalev, V.D. Neverov, Y.V. Zhumagulov, A.V. Krasavin, D. Kochan, Strength of the hubbard potential and its modification by breathing distortion in $babio_3$, Phys. Rev. B 105 (2022) 045131, 10.

[52] R.L. Bouwmeester, K. de Hond, N. Gauquelin, J. Verbeeck, G. Koster, A. Brinkman, Stabilization of the perovskite phase in the Y–Bi–O system by using a $BaBiO_3$ buffer layer, Phys. Status Solidi (RRL) 13 (7) (2019) 1800679.

[53] T.L. Barr, S. Seal, Nature of the use of adventitious carbon as a binding energy standard, J. Vacuum Sci. Technol. A: Vacuum SurfacesFilms 13 (3) (1995) 1239–1246.

[54] M. Zapf, M. Stübinger, L. Jin, M. Kamp, F. Pfaff, A. Lubk, B. Büchner, M. Sing, R. Claessen, Domain matching epitaxy of $BaBiO_3$ on $SrTiO_3$ with structurally modified interface, Appl. Phys. Lett. 112 (14) (2018) 141601.

[55] L. Jin, M. Zapf, M. Stübinger, M. Kamp, M. Sing, R. Claessen, C.L. Jia, Atomic-scale interface structure in domain matching epitaxial $BaBiO_3$ thin films grown on $SrTiO_3$ substrates, Phys. Status Solidi (RRL) 14 (n/a) (2020) 2000054.

[56] D. Xiao, W. Zhu, Y. Ran, N. Nagaosa, S. Okamoto, Interface engineering of quantum Hall effects in digital transition metal oxide heterostructures, Nature Commun. 2 (2011) 596.

[57] Y. Weng, X. Huang, Y. Yao, S. Dong, Topological magnetic phase in $LaMnO_3$ (111) bilayer, Phys. Rev. B 92 (2015) 195114.

[58] O. Köksal, R. Pentcheva, Chern and $\mathbb{Z}_2$ topological insulating phases in perovskite-derived 4D and 5D oxide buckled honeycomb lattices, Sci. Rep. 9 (1) (2019) 1–11.

[59] M.M. Qazilbash, M. Brehm, B.-G. Chae, P.-C. Ho, G.O. Andreev, B.-J. Kim, S.J. Yun, A. Balatsky, M. Maple, F. Keilmann, et al., Mott transition in VO_2 revealed by infrared spectroscopy and nano-imaging, Science 318 (5857) (2007) 1750–1753.